Design and Analysis of Unevenly Spaced Split-tooth Permanent-Magnet Vernier Motor for Low Cogging Torque

Jingfeng Mao, Xinyu Xu, Yujie Tang, Yongqiang Ren, Jingyun Feng, and Junqiang Zheng*

School of Electrical Engineering and Automation, Nantong University, Nantong 226019, China

(Received 14 June 2024, Received in final form 4 January 2025, Accepted 6 January 2025)

This paper proposes a novel rectangular modulated tooth arrangement suitable for Permanent-Magnet Vernier (PMV) motors. The proposed special arrangement of modulated teeth can significantly reduce the machine cogging torque while maintaining torque density without added complexity. Firstly, a theoretical model of cogging torque generation in unevenly spaced split-tooth (USST) PMV motors is derived, and a mathematical relationship between the modulated tooth structure and cogging torque is established. Then, a 20-slot, 62-pole PMV motor is optimized and compared to a traditional modulated tooth arrangement. Finally, a finite-element model is used to analyze the torque, cogging torque, and losses. The results demonstrate the effectiveness of the new arrangement in reducing cogging torque.

Keywords: cogging torque, torque ripple, non-uniform modulation teeth, permanent magnet vernier motor

1. Introduction

Due to their superior low-speed high-torque performance, the Permanent-Magnet Vernier (PMV) motors hold significant potential for applications in wind power generation, marine propulsion, and oil field extraction [1]. Currently, the research on PMV motors focuses on the synergistic enhancement of torque density and power factor, alongside loss suppression [2]. However, there is a scarcity of literature devoted to reducing the cogging torque and torque ripple in PMV motors, even though it is well known that PMV motors develop significant cogging torque because of their strong no-load magnetic field [3].

Cogging torque control is vital in Permanent-Magnet (PM) motors. It is caused by the interaction between the PMs and the stator core when the motor windings are unenergized [4]. Cogging torque produces noise and vibration, particularly at low speeds [5, 6]. Due to their high torque density and low speeds, PMV motors are often used in direct electric drive systems [7]. However, their low-speed operation and complex modulated tooth arrangements exacerbate the cogging torque issue, necessitating the need to study the cogging torque in PMV motors for improved stability of direct electric drive

systems [8].

The existing approaches to reducing cogging torque include altering the quantity and configuration of PMs [9], modifying the modulation teeth amplitude [10, 11], and utilizing unevenly spaced split-tooth (USST) arrangements [12, 13]. The USTS-PMV motors maintain a constant number of modulation teeth while splitting the modulation teeth into sets, each comprising at least two teeth. Research demonstrated that by modifying the duty cycle of the modulation teeth or the relative positioning of each set of modulation teeth, it is possible to effectively reduce the magnetic resistance of the working subharmonic flux paths. This reduction, in turn, enhances the amplitude of the working sub-harmonics and yields better torque density [14-16].

The USST-PMV motors exhibit good low-speed, high-torque characteristics. However, compared to the high-torque-density magnetic field modulation motors with multi-layer air gaps, their torque density is still inferior. Moreover, the increased cogging torque ripple negatively affects system stability and elevates noise [17]. This study analyzes theoretically the relationship between the non-equidistant modulation tooth arrangement and cogging torque in USST-PMV motors, considering the pole-changing modulation and field-circuit collaboration. Finite-element method (FEM) simulations are conducted to verify the correctness of theoretical results [18-21].

©The Korean Magnetics Society. All rights reserved.

*Corresponding author: Tel: +86-15190823468

e-mail: zjq@ntu.edu.cn

This structure of this paper is organized as follows: Section 2 presents the new modulated tooth design, highlighting the differences from the existing modulated tooth arrangements. Section 3 analyzes the mechanism by which modifications in the modulated tooth arrangement alter the air gap permeance, thereby achieving suppression of cogging torque. Sections 4 and 5 validate the effectiveness of the new modulated tooth design in suppressing cogging torque via finite element analysis of a 62-pole, 20-slot PMV motor with different modulated tooth designs.

2. Structure and Characteristics of Unevenly Spaced Split-tooth Arrangement

The modulation tooth arrangement in an evenly spaced split-tooth (ESST) PMV motor is shown in Fig. 1 (I). For each modulation tooth, the angles of the modulation and stator slot openings are equal (hereinafter referred to as Structure I). Structure I splits two virtual tooth structures on the same stator tooth, with the split teeth acting as modulation poles. This structure increases the frequency of the main working harmonics, thereby enhancing the torque density. An existing USST-PMV motor with exhibits enhanced torque performance is shown in Fig. 1 (II) (hereinafter referred to as Structure II). In this arrangement, the modulation teeth are grouped in pairs. For Structure II, the relationship between the modulation tooth slot angle α^* , the modulation tooth slot opening angle β^* , and the slot opening angle γ^* is $\beta^* + \gamma^* = 2\alpha^*$. Although Structure II improves torque density, it exacerbates magnetic flux leakage and worsens losses. A USST-PMV motor with modulation teeth arranged in sets of four is illustrated in Fig. 1 (III) (hereinafter referred to as Structure III). For Structure III, the relationship between angles α^* (the modulation tooth slot), β^* (the slot opening angle of the second slot in each tooth set and the modulation tooth slot opening), and γ^* (the slot opening angle of the first slot in each set) is $3\beta^* + \gamma^* = 4\alpha^*$. Related studies indicate that by altering the relative positions of the modulation teeth within each set, it is possible to effectively reduce the magnetic resistance of the working harmonic magnetic flux paths. This means that by increasing the amplitude of the working harmonic, it is possible to enhance the torque density. The amplitude of cogging torque is primarily determined by the air gap permeance, while its periodicity is dictated by the alignment between the stator teeth and PMs. Therefore, by analyzing the effect of the modulated tooth arrangement on air gap permeance, it is possible to determine whether it can suppress cogging torque and identify the specific structural parameters required for this suppression. The following section will analyze the air gap permeance of the three structures.

3. Principle of Cogging Torque Reduction

To demonstrate the performance of USST arrangement in reducing the cogging torque in PMV motors, the following discussion utilizes the basic theories of pole-changing modulation and magnetic circuit cooperation to derive a theoretical relationship between the USST arrangement and the cogging torque in PM motors.

By substituting the Fourier expression for the magnetic conductivity function of the split-tooth PMV motor into the expression for cogging torque, the following relationship between the cogging torque and air gap permeance G_n can be obtained:

$$T_{cogging}(\alpha) = k \sum_{m=1}^{\infty} nG_n f(\alpha)$$
 (1)

where,

$$k = \frac{\pi Z L_a (R_2^2 - R_1^2)}{8\mu_0} \tag{2}$$

$$f(\alpha) = \sin[LCM(Z, 2p)\alpha] \tag{3}$$

In Equations (2) and (3), L_a is the axial length of the armature core, R_1 and R_2 respectively represent the inner

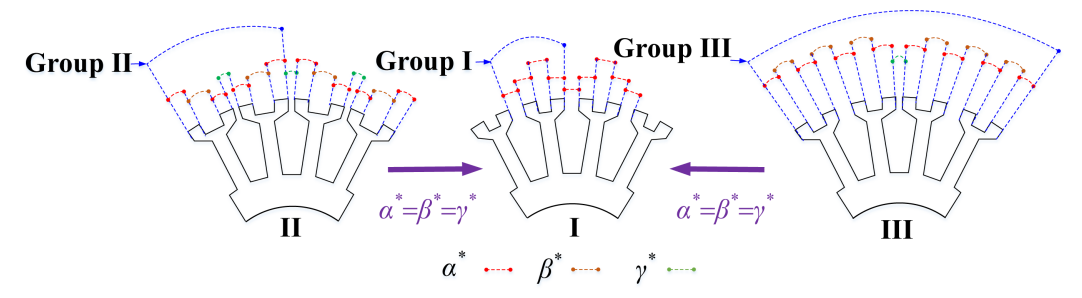


Fig. 1. (Color online) Different Modulation tooth structure I, II and III.

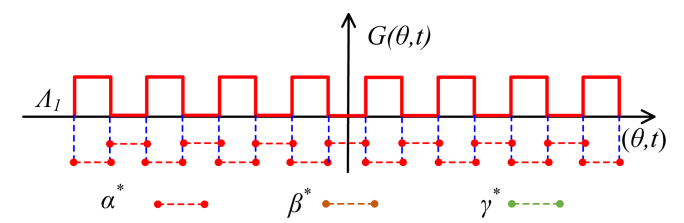


Fig. 2. (Color online) Airgap permeance function of modulation tooth I.

and outer diameters of the motor. n is the harmonic order of the air gap permeance that affects the cogging torque, Z is the number of armature teeth, and α is the electrical angle between the stator and rotor.

The magnetic conductivity model of the ESST arrangement of Structure I is shown in Fig. 2. The expression for its magnetic conductivity is as follows:

$$G_n(I) = \frac{4G_1}{n\pi} \left[\sin(\frac{n\pi}{4}) - \sin(\frac{5n\pi}{4}) \right]$$
 (4)

For the ESST arrangement of PMV motors, the cogging torque is minimized only when n=1, 3, 5, 7, 21, 35, 37, 91, 95, ...

Analyzing the air gap permeance model of the USST arrangement in Structure II, shown in Fig. 3, yields the following expression for the motor air gap permeance:

$$G_n(II) = \frac{4G_1}{n\pi} \left[\sin(\frac{nZ\gamma^*}{2}) - \sin(\frac{3n\pi}{2} - \frac{nZ\gamma^*}{2}) \right]$$
 (5)

The relationships between β , β^* , γ , γ^* and α for Structure II can be expressed as follows:

$$\begin{cases} \beta^* = \beta_2, \gamma^* = \gamma_2 \\ \beta_2 + \gamma_2 = 2\alpha \end{cases}$$
 (6)

The motor air gap permeance model for the modulation tooth Structure III is shown in Fig. 4. The expression for the motor air gap permeance is as follows:

$$G_n(III) = \frac{4G_1}{n\pi} \left(\sin\left(\frac{5n\pi}{6} - \frac{nZ\gamma^*}{12}\right) - \sin\left(\frac{7n\pi}{12} + \frac{nZ\gamma^*}{12}\right) \right)$$
 (7)

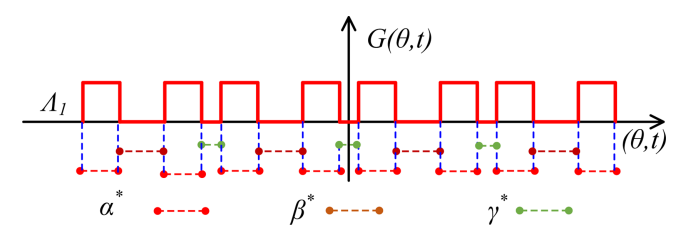


Fig. 3. (Color online) Airgap permeance function of modulation tooth II.

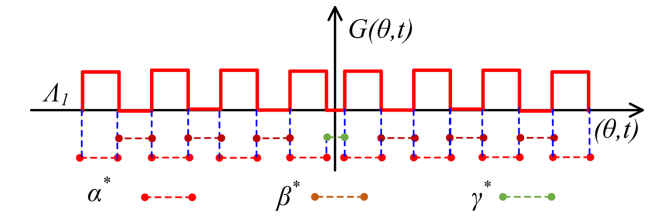


Fig. 4. (Color online) Airgap permeance function of modulation tooth III.

The relationships between β , β^* , γ , γ^* and α in Structure III can be expressed as follows:

$$\begin{cases} \beta^* = \beta_3, \gamma^* = \gamma_3 \\ 3\beta_3 + \gamma_3 = 4\alpha \end{cases}$$
 (8)

From Equations (5) and (7), the air gap permeance G_n vanishes in a USST-PMV motor for certain angles. Even if n is not the value that minimizes the cogging torque of Structure I, it can still be effectively reduced by adjusting angle γ^* .

4. Finite-element Validation

To validate the accuracy of the theoretical results, models of PMV motors with 62 poles and 20 slots were created (motor parameters are listed in Table 1) using FEM. The models for Structures I, II, and III are shown in Fig. 1. Note that when $\alpha^*=4.5^{\circ}$ for Structures II and III, their motor modulation tooth arrangement becomes identical to that of Structure I. The motor structure is shown in Fig. 5.

Fig. 6 compares the back electromotive force (back-EMF) of the three different modulation tooth arrangements, while their harmonic spectra are shown in Fig. 7.

Table 1. Parameters of USS-PMV motor.

Parameters	Value
Number of slots, N _s	20
Pole pairs of PMs, P _r	31
Number of modulation teeth, N _{st}	40
Stator outer diameter, D _o (mm)	70
Rotor outer diameter, D _o (mm)	60
Length, L _s (mm)	60
Air gap thickness, d (mm)	0.5
Thickness of PMs, H _{pm} (mm)	2
Angle of the tolerance teeth, $\alpha^*(deg)$	4.5
Width of the armature teeth, L(mm)	6.25
Pole arc coefficient	1
Number of turns per coil per slot, N _{tum}	42

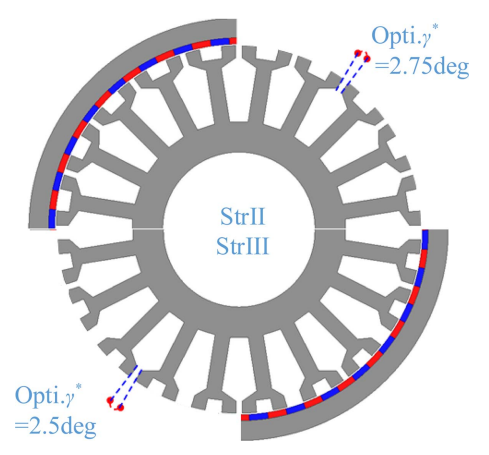


Fig. 5. (Color online) Optimal motor's structure of modulation tooth II and III.

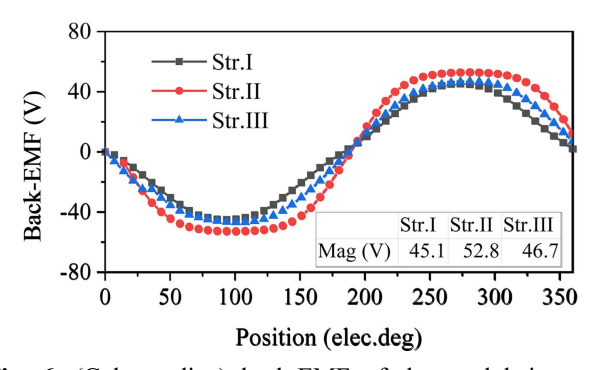


Fig. 6. (Color online) back-EMF of the modulation tooth structures I, II and III.

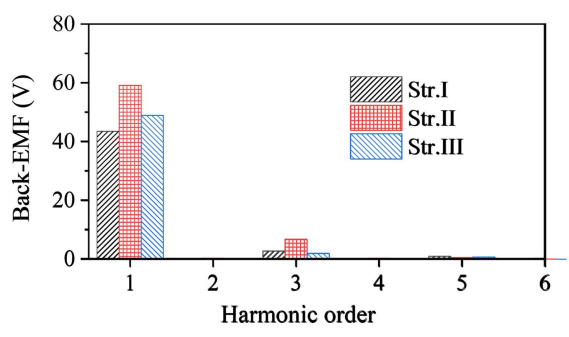


Fig. 7. (Color online) Harmonic spectra of structures I, II and III.

It can be observed that the variations in the stator modulation teeth arrangement slightly modify the back-EMF. Structure II exhibits the highest back-EMF, while Structure III shows only a slight improvement in the back-EMF.

Overall, the different modulation tooth arrangements have minimal impact on the waveform of the motor open-circuit EMF.

At the peaks of the evenly spaced teeth, the waveform

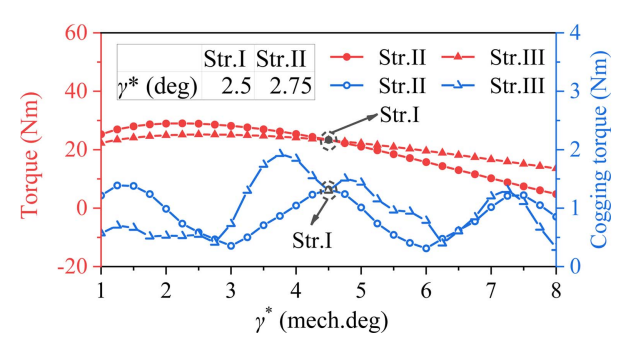


Fig. 8. (Color online) Cogging torque and average torque of structures I, II and III.

exhibits a sharp peak and appears more sinusoidal. The peak values of the back-EMF are approximately 45.1 V. The back-EMF of USST motor slightly increases.

For Structure II, the fundamental amplitude increases from 45.1 V to 52.8 V, i.e., by 17%, whereas for Structure III from 45.1 V to 46.7 V, i.e., by 3.5%.

The cogging torque and average torque of Structures II and III are compared in Fig. 8 The trends of the average torque with respect to the stator slot opening angle are essentially the same. However, the average torque of Structure III is overall lower than that of Structure II but higher than that of Structure I. Even though it is not at the

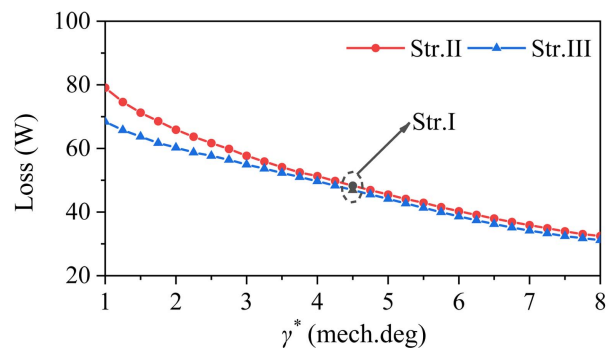


Fig. 9. (Color online) Iron loss of structures II and III.

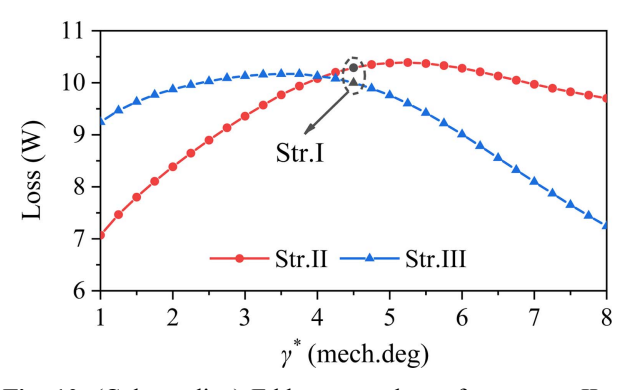


Fig. 10. (Color online) Eddy-current loss of structures II and III.

optimal point for torque performance, both structures exhibit only minimal torque ripple around γ^* of approximately 2.5-2.8°.

Fig. 9 exhibits the iron loss of both structures under rated load conditions. It can be observed that the iron loss

of Structure III is slightly reduced. At the optimal torque point of 2.5° for Structure II and 2.75° for Structure III, the iron loss of Structure III decreases from 63.7 W to 58.7 W compared to Structure II, representing a reduction of approximately 8%.

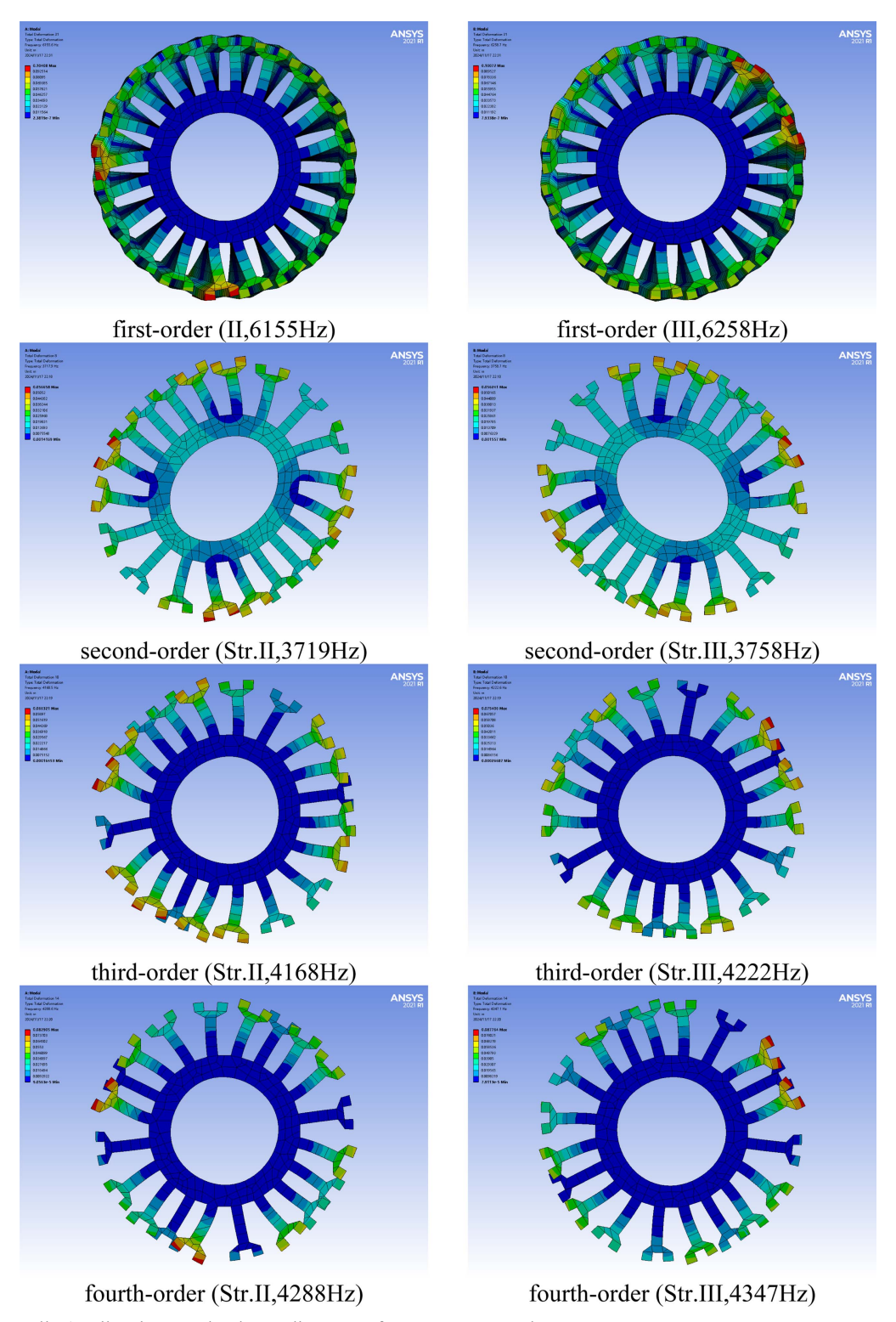


Fig. 11. (Color online) Vibration mode shape diagram of structures II and III.

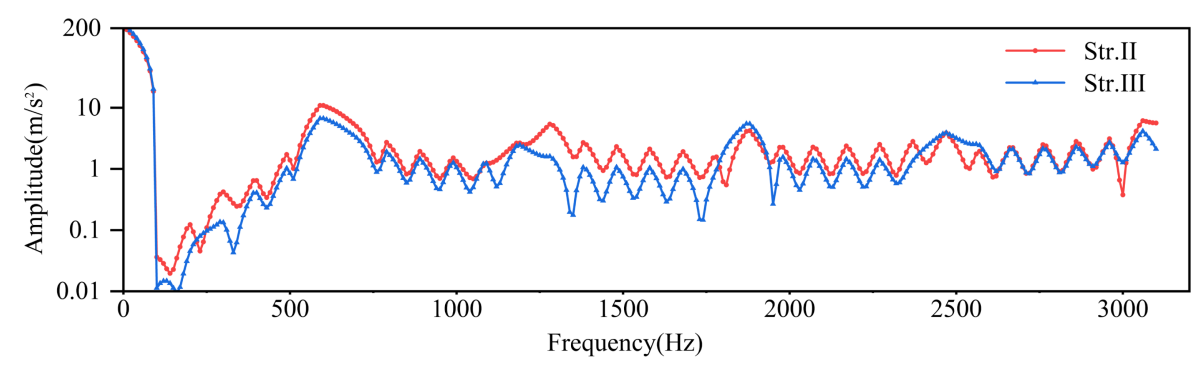


Fig. 12. (Color online) Motor vibration acceleration at 600 rpm with load of structures II and III.

The eddy-current losses of both structures are presented in Fig. 10, where it can be observed that the eddy-current loss of Structure III is slightly higher than that of Structure II. At the optimal torque point of 2.5°, the eddy-current loss of Structure III is 9.9 W, which is 1.3 W higher compared to the optimal eddy-current loss of Structure II at 2.7°.

The total loss of Structure III is 68.6 W, and the loss of Structure II is 72.3 W, representing a decrease of approximately 5.1%.

FEM simulations were conducted to examine the structural modes of the stator to prevent resonance occurrence and accurately predict the electromagnetic vibration noise of the motor. The modal shapes and lower-order intrinsic frequencies of the stator were calculated, assuming that the stacking effects can be ignored and the coil can be treated as accessory mass. The results are presented in Fig. 11. Notably, the secondorder resonance frequencies, which exhibit the lowest intrinsic frequencies, were determined to be 3,719 Hz for Structure II and 3,758 Hz for Structure III. The resonance frequencies of both structures were significantly distant from the operating frequency of 310 Hz at a rotational speed of 600 rpm. The second-order resonance frequency of Structure III was slightly higher than that of Structure II, indicating a marginally better performance.

Fig. 12 presents the radial acceleration spectra of the two structures at 600 rpm under load. Significant vibrations occur at even harmonics of the motor fundamental frequency (310 Hz). Structure III demonstrates lower radial acceleration than Structure II across most frequencies, indicating superior performance.

5. Conclusions

In this study, the principle of torque reduction by a novel USST arrangement was theoretically analyzed, and the USST design was optimized. Compared to the original structure, the average torque of the proposed new arrangement increased by approximately 8.3%. Compared to the existing ESST-PMV motors, the new structure achieved a cogging torque reduction of approximately 69%. Compared to the existing USST-PMV motors, the loss dropped by approximately 5%.

The accuracy of the analytical results was validated using an FEM model. Subsequently, the USST arrangement was optimized to further reduce cogging torque and increase torque. The optimization results indicated the optimal performance when the armature tooth width was 6.25 mm, the modulation slot depth was 2 mm, and the modulation angle was 2.75°. At this point, the cogging torque was 0.41 Nm (approximately 2.1%), and the torque was 25.19 Nm. Moreover, the resonance performance of the novel tooth arrangement surpassed that of the traditional one.

Acknowledgments

This work was supported by the National Natural Science Foundation of China (52307061), the National Science Research Program of Jiangsu Colleges and Universities under Grant (23KJB470033), and the Postgraduate Research & Practice Innovation Program of Jiangsu Province (SJCX24 2005).

References

- [1] C. Gong and F. Deng, IEEE Trans. Ind. Electron. **69**, 5421 (2022).
- [2] Y. Yu, Y. Pei, F. Chai, and M. Doppelbauer, IEEE Trans. Ind. Electron. **70**, 7761 (2023).
- [3] F. Yan, J. Ji, Z. Ling, Y. Sun, and W. Zhao, Chinese J. Electr. Eng. **8**, 90 (2022).
- [4] H. Chen, N. A. O. Demerdash, A. M. EL-Refaie, Y. Guo, W. Hua, and C. H. T. Lee, IEEE Trans. Energy Convers. 37, 1442 (2022).

- [5] H.-K. Lee, J.-H. Woo, H.-S. Shin, K.-H. Shin, and J.-Y. Choi, J. Magn. 25, 485 (2020).
- [6] L. Dang, N. Bernard, N. Bracikowski, and G. Berthiau, IEEE Trans. Ind. Electron. 64, 9834 (2017).
- [7] H. Huang, D. Li, X. Ren, and R. Qu, IEEE Trans. Ind. Appl. 58, 4637 (2022).
- [8] J.-H. Lee and Y.-S. Park, J. Magn. 23, 267 (2018).
- [9] S.-H. Lee, J.-Y. Kim, and D.-W. Kang, J. Magn. **24**, 362 (2019).
- [10] Z. Q. Zhu and D. Howe, IEEE Trans. Energy Convers. **15**, 407 (2000).
- [11] F. Yang, Y. Xie, and W. Cai, IEEE Trans. Magn. 57, 1 (2021).
- [12] T. Zou, D. Li, R. Qu, D. Jiang, and J. Li, IEEE Trans. Ind. Appl. 53, 5295 (2017).
- [13] L. Fang, D. Li, X. Ren, and R. Qu, IEEE Trans. Ind. Electron. **69**, 6058 (2022).

- [14] K. Atallah and D. Howe, Trans. Magn. 37, 2844 (2001).
- [15] L. Xu, W. Wu, and W. Zhao, IEEE Trans. Ind. Electron. **69**, 12281 (2022).
- [16] R. Li, C. Shi, R. Qu, D. Li, X. Ren, V. Fedida, and Y. Zhou, IEEE Trans. Magn. 57, 1 (2021).
- [17] L. Xu, Y. Li, W. Zhao, and G. Liu, CES Transactions on Electrical Machines and Systems 7, 35 (2023).
- [18] S. Khan, F. Khan, W. Ullah, Z. Ahmad, and B. Ullah, IEEE Access 10, 75672 (2022).
- [19] T. Zou, D. Li, R. Qu, D. Jiang, and J. Li, IEEE Trans. Ind. Appl. 53, 5295 (2017).
- [20] H. Huang, D. Li, X. Ren, and R. Qu, IEEE Trans. Ind. Appl. **58**, 4637 (2022).
- [21] M. Ghods, J. Faiz, H. Gorginpour, M. A. Bazrafshan, and J. K. Nøland, IEEE Transactions on Transportation Electrification **9**, 3880 (2023).